Fluorinated naphtho[1,2-*c*:5,6-*c'*]bis[1,2,5] thiadiazole-containing π-conjugated compound: synthesis, properties, and acceptor applications in organic solar cells

Shreyam Chatterjee[1], Yutaka Ie [1,2], Takuji Seo[1], Taichi Moriyama[3], Gert-Jan A. H. Wetzelaer[2], Paul W. M. Blom[2] and Yoshio Aso[1]

Abstract

The incorporation of electron-accepting units into π-conjugated systems is well-established as a powerful approach to tune the physical properties and frontier orbital energy levels of molecules. To realize semiconductors with novel functions, naphtho[1,2-*c*:5,6-*c'*]bis[1,2,5]thiadiazole (**NTz**) has been utilized as an effective electron-accepting unit. To enhance the electron-accepting nature of **NTz** in this work, the synthesis of fluorinated naphthobisthiadiazole (**FNTz**) was accomplished by the sequential introduction of amino functional groups into 1,5-difluoronapthalene derivatives to form fluorinated tetraaminonapthalene derivatives, followed by the formation of thiadiazole rings. Organic solar cells based on our synthesized **FNTz** acceptor in combination with poly(3-hexylthiophene) (P3HT) as a donor exhibit a significant improvement of power conversion efficiency (PCE) compared to the corresponding nonfluorinated **NTz**-based cells, reaching a high PCE of up to 3.12%. Investigation of the blend-film properties and device physics unambiguously reveals that the blend films based on P3HT and the **FNTz**-based compound shows good film morphologies and thus efficient charge generation and transport characteristics. These results demonstrate the potential of **FNTz** for an electron-accepting unit in organic semiconductors.

Introduction

π-Conjugated systems have established indispensable positions as semiconducting materials in organic electronics, such as organic light-emitting diodes, field-effect transistors, and organic solar cells (OSCs).[1] One of the great advantages of organic semiconductors is the potential to adjust the highest occupied molecular orbital (HOMO) and lowest unoccupied molecular orbital (LUMO) energy levels, enabling tuning of the relative energies between the frontier orbitals of organic

semiconductors and the Fermi level of metal electrodes. Thus, selective injection and transportation of holes and/or electrons can be achieved, which is essential for the realization of such organic devices.[2–5] In this context, it is generally recognized that the incorporation of an electron-accepting unit into the π-conjugated system is an effective approach to tune the HOMO and LUMO energy levels. However, given that effective electron-accepting units are still limited,[6–11] the creation of novel electron-accepting units is strongly needed to boost the development of high-performance organic semiconductors.

Naphtho[1,2-*c*:5,6-*c'*]bis[1,2,5]thiadiazole (**NTz**), a doubly 2,1,3-benzobisthiadiazole (**BTz**)-fused heteroaromatic molecule, has been known to function effectively as an electron-accepting unit of donor–acceptor type donor copolymers for bulk-heterojunction OSCs (Fig. 1).[12–16]

Correspondence: Yutaka Ie (yutakaie@sanken.osaka-u.ac.jp)
[1]The Institute of Scientific and Industrial Research, Osaka University, 8-1 Mihogaoka, Ibaraki, Osaka 567-0047, Japan
[2]Max Planck Institute for Polymer Research, Ackermannweg 10, 55128 Mainz, Germany
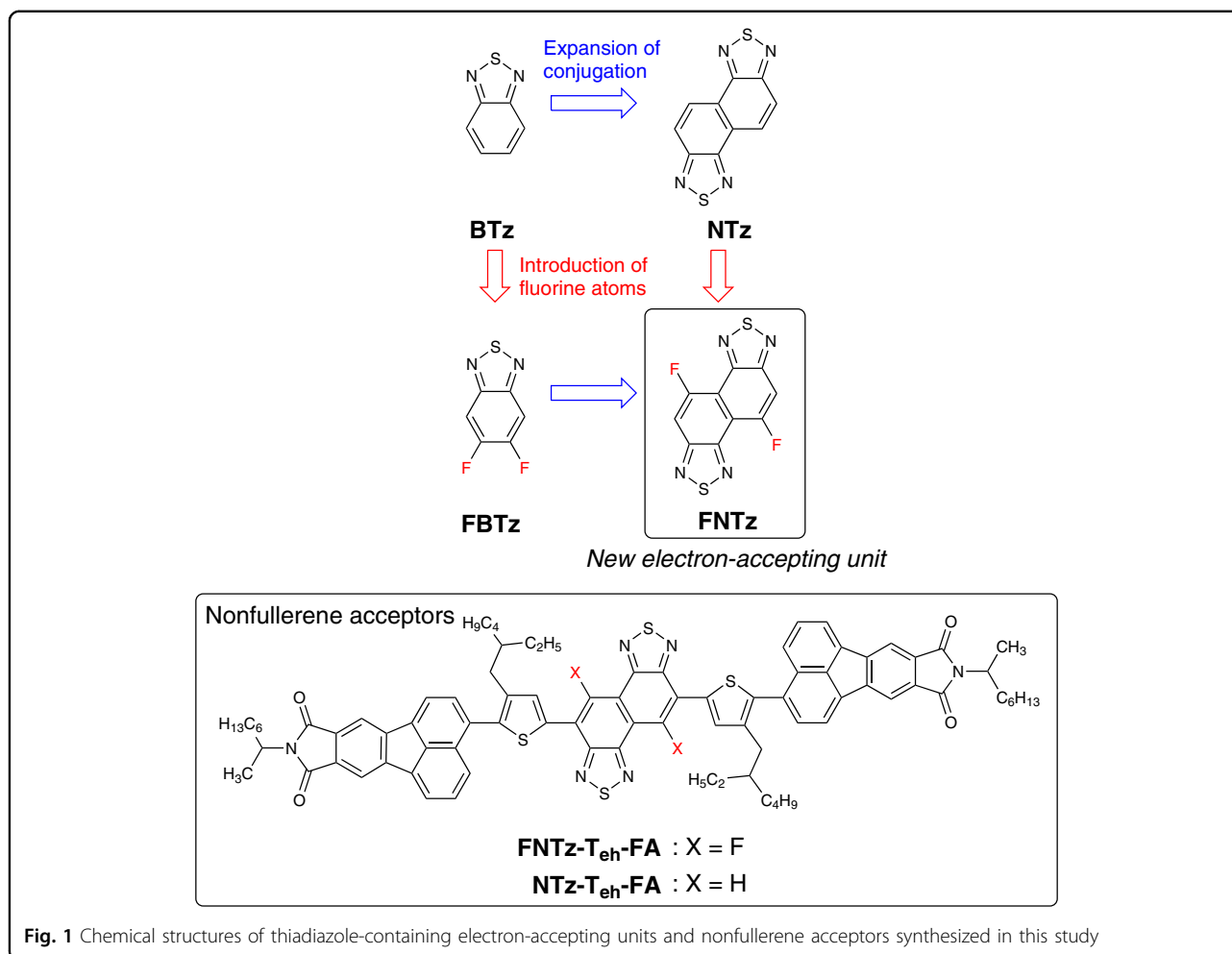Full list of author information is available at the end of the article.

Fig. 1 Chemical structures of thiadiazole-containing electron-accepting units and nonfullerene acceptors synthesized in this study

Recently, we have reported that **NTz** can also be applied as the electron-accepting unit in nonfullerene acceptors and revealed that the **NTz**-containing acceptors contribute to lowering the LUMO energy level and enhancing the overall performance of OSCs compared to the corresponding **BTz**-based molecules.[17–20] These results show that the chemical modification of **NTz** toward a stronger electron-accepting character is a straightforward direction to enhance device performance, since this modification can reduce the band gap, as well as lower the LUMO energy level of the resulting π-conjugated systems. As further development of this strategy, we introduce strongly electron-withdrawing fluorine atoms into the **NTz** ring and synthesized **FNTz** as a new electron-accepting unit (Fig. 1). In a similar approach, the fluorinated benzobisthiazole (**FBTz**) was developed to increase the electron-accepting character of **BTz**, and a donor−acceptor type donor copolymer containing **FBTz** showed superior photovoltaic performance to the corresponding **BTz**-based copolymer.[21–24] Furthermore, fluorine-containing compounds are expected to have unique intermolecular interactions.[25] In this contribution, we developed a structurally well-defined nonfullerene acceptor **FNTz-T$_{eh}$-FA**, whose structure consists of the pivotal fluorinated **FNTz**, 2-ethylhexyl-substituted thiophene (**T$_{eh}$**), and fluoranthene imide (**FA**) as central, linker, and terminal units, respectively. Furthermore, the influence of the fluorine atoms on the properties and photovoltaic performance was examined in a direct comparison with **NTz-T$_{eh}$-FA**.

Materials and methods
General information

Column chromatography was performed on silica gel (40–50 μm). Thin-layer chromatography plates were visualized with UV light. Preparative GPC was performed on a Japan Analytical Industry LC-918 equipped with JAI-GEL 1H/2H. ^{1}H and ^{13}C NMR spectra were recorded on a JEOL ECS-400 spectrometer in deuterated solvent with tetramethylsilane (TMS) as an internal standard. Data are reported as follows: chemical shift in ppm (δ), multiplicity (s = singlet, d = doublet, t = triplet, m = multiplet,

br = broad), and coupling constant (Hz). Mass spectra were obtained on a Shimadzu GCMS-QP-5050 or Shimadzu AXIMA-TOF. High-resolution mass spectra (HRMS) were obtained via atmospheric pressure chemical ionization (APCI) using a Thermo scientific LTQ Orbitrap XL. Elemental analysis was performed on a Perkin Elmer LS-50B by the Elemental Analysis Section of the Comprehensive Analysis Center (CAC), ISIR, Osaka University.

Thermogravimetric (TGA) analysis and differential scanning calorimetry (DSC) were performed under nitrogen at a heating rate of $10\,^{\circ}\mathrm{C}\,\mathrm{min}^{-1}$ with a Shimadzu TGA-50 and a Shimadzu DSC-60, respectively. UV-vis spectra were recorded on a Shimadzu UV-3600 spectrophotometer. Cyclic voltammetry (CV) and differential pulse voltammetry (DPV) were carried out on a BAS CV-620C voltammetric analyzer using a platinum disk as the working electrode, platinum wire as the counter electrode, and $\mathrm{Ag/AgNO_3}$ as the reference electrode at a scan rate of $100\,\mathrm{mV\,s^{-1}}$. Photoelectron spectroscopy in air (PESA) was carried out using a Riken Keiki Co. Ltd. AC-3 with a light intensity of 20 mW. Fluorescence spectra were recorded using a Fluoromax-4 spectrometer in the photo-counting mode equipped with a Hamamatsu R928P photomultiplier. The bandpass for the emission spectra was 1.0 nm. All spectra were obtained in spectrograde solvents. The surface structures of the deposited organic films were observed by atomic force microscopy (AFM) (Shimadzu, SPM9600). X-ray diffraction (XRD) patterns were obtained using Bragg-Brentano geometry with Cu Kα radiation as an X-ray source with an acceleration voltage of 45 kV and a beam current of 200 mA. The scanning mode was set to $2\theta-\theta$ scans between 2° and 30° with scanning steps of 0.01°.

Synthesis of 2

To a stirred solution of **1** (3.00 g, 18.3 mmol) and tri-fluoroacetic acid (25 mL) in a 100 mL round-bottom flask was added *N*-bromosuccinimide (NBS) (7.81 g, 43.9 mmol) at room temperature. After stirring for 16 h at 70 °C, the reaction mixture was quenched by the addition of water. After removal of the solvent by filtration, the residue was washed with methanol to give compound **2** (5.70 g, 97%) as a gray solid. ^{1}H NMR (400 MHz, CDCl$_3$, δ): 7.79–7.76 (m, 2H), 7.14–7.09 (m, 2H); MS (EI) *m/z* 321 (M$^+$); Anal. calcd for C$_{10}$H$_4$Br$_2$F$_2$: C 37.31, H 1.25; found: C 37.46, H 1.53.

Synthesis of 3

Compound **2** (1.93 g, 6.00 mmol), benzophenone imine (2.61 g, 14.4 mmol), Pd$_2$(dba)$_3$·CHCl$_3$ (312 mg, 0.30 mmol), *rac*-2,2′-bis(diphenylphosphino)-1,1′-binaphthyl (*rac*-BINAP) (186 mg, 0.30 mmol), and sodium *t*-butoxide (507 mg, 24.0 mmol) were placed in a pressure vessel and dissolved with toluene (30 mL). The reaction mixture was refluxed for 5 h. After removal of the solvent under reduced pressure, the mixture was cooled to room temperature. The reaction mixture was filtered over celite and washed with ethyl acetate (EtOAc). After removal of the solvent under reduced pressure, the residue was purified by column chromatography on silica gel (hexane/EtOAc = 1/1) to give intermediate **A**. ^{1}H NMR (400 MHz, CDCl$_3$, δ): 7.78–7.76 (m, 4H), 7.50–7.38 (m, 6H), 7.21–7.10 (m, 6H), 7.05–7.02 (m, 4H), 6.81 (dd, $J = 13.2$, 8.4Hz, 2H), 6.37 (dd, $J = 8.4$, 4.0Hz, 2H).

To a stirred solution of **A** and THF (45 mL) was added 2 M HCl aq. (9 mL) at 0 °C. Then, this mixture was stirred at 0 °C for 1 h. After removal of the solvent by filtration, the residue was washed with THF to give compound **3** (986 mg, 62% (2 steps)) as a dark yellow solid. ^{1}H NMR (400 MHz, DMSO-d_6, δ): 7.26–7.21 (m, 2 H), 7.13 (br, 2 H), 3.87–3.69 (br, 4 H); MS (EI) *m/z* 267 (M$^+$); Anal. calcd for C$_{10}$H$_4$Cl$_2$F$_2$N$_2$: C 44.97, H 3.77, N 10.49; found: C 45.00, H 3.97, N 10.23.

Synthesis of 4

Compound **3** (2.20 g, 8.24 mmol) was placed in a 300 mL round-bottom flask and dissolved with CH$_2$Cl$_2$ (100 mL). To the mixture was added triethylamine (3.34 g, 33.0 mmol) and trifluoroacetic anhydride (8.65 g, 41.2 mmol) at 0 °C. The mixture was gradually warmed to room temperature and stirred overnight. After removal of the solvent under reduced pressure, the residue was filtered and washed with MeOH to give **4** (2.91 g, 91%) as a white solid. ^{1}H NMR (400 MHz, acetone-d_6, δ): 10.45 (s, 2 H), 7.84–7.79 (m, 2 H), 7.53–7.48 (m, 2 H); ^{13}C NMR (100 MHz, acetone-d_6, δ): 157.1 (d, $J = 252$ Hz), 156.0 (d, $J = 37.2$ Hz), 127.0 (d, $J = 11.4$ Hz), 125.6, 121.7, 116.3 (q, $J = 287$ Hz), 113.1 (d, $J = 23.8$ Hz); MS (EI) *m/z* 386 (M$^+$); Anal. calcd for C$_{14}$H$_6$F$_8$N$_2$O$_2$: C 43.54, H 1.57, N 7.25; found: C 43.43, H 1.77, N 7.38.

Synthesis of 5

Compound **4** (386 mg, 1.00 mmol) was placed in a 50-mL round-bottom flask and dissolved with conc. H$_2$SO$_4$ (8 mL). To the mixture was added HNO$_3$ (2.0 mL) at −45 °C, and the mixture stirred for 5 min. The reaction mixture was poured into ice and extracted with EtOAc. After removal of the solvent under reduced pressure, the residue was filtered and washed with diethyl ether to give **5** (368 mg, 77%) as a dark orange solid. ^{1}H NMR (400 MHz, acetone-d_6, δ): 10.97 (s, 2 H), 8.33–8.29 (m, 2 H); ^{13}C NMR (100 MHz, acetone-d_6, δ): 158.9 (d, $J = 257$ Hz), 156.5 (d, $J = 38.2$ Hz), 146.9, 124.5, 119.9, 115.9 (q, $J = 286$ Hz), 111.3 (d, $J = 31.4$ Hz); MS (EI) *m/z* 476 (M$^+$); Anal. calcd for C$_{14}$H$_4$F$_8$N$_4$O$_6$: C 35.31, H 0.85, N 11.77; found: C 35.08, H 1.18, N 11.45.

Synthesis of FNTz

Compound **5** (238 mg, 0.50 mmol) was placed in a 100 mL round-bottom flask and dissolved with MeOH (20 mL). To the mixture was added conc. HCl (10 mL) at room temperature, and the mixture was stirred at 90 °C overnight. After removal of the solvent under reduced pressure, the residue was filtered and washed with conc. HCl and CH_2Cl_2 to give intermediate **B** (129 mg). ^{1}H NMR (400 MHz, DMSO-d_6, δ): 8.15 (s, 4 H), 7.94–7.90 (m, 2 H).

Intermediate **B** (246 mg, 0.69 mmol) was placed in a 50-mL round-bottom flask and dissolved with conc. HCl (25 mL). To the mixture was added $SnCl_2$ (2.62 g, 13.8 mmol) at 0 °C, and the mixture was stirred for 1 h. After filtration, the residue was washed with conc. HCl and CH_2Cl_2 to give intermediate **C** (240 mg). ^{1}H NMR (400 MHz, DMSO-d_6, δ): 9.00–7.00 (br), 6.96 (d, 2 H, J = 15.6 Hz).

Intermediate **C** (174 mg, 0.47 mmol) was placed in a 100 mL round-bottom flask and dissolved with pyridine (18 mL). To the mixture was added thionyl chloride (1.12 g, 9.40 mmol) at room temperature, and stirring continued at 90 °C for 2 h. After removal of the solvent under reduced pressure, the residue was filtered and washed with MeOH to give **FNTz** (130 mg, 67% (3 steps)) as a brown solid. ^{1}H NMR (400 MHz, CDCl$_3$, δ): 8.06–8.01(m, 2 H); MS (EI) *m/z* 280 (M$^+$); HRMS (APCI) *m/z*: [M + H]$^+$ calcd for $C_{10}H_2F_2N_4S_2$, 279.9689, found, 280.9762.

Synthesis of FNTz-Br

To a stirred solution of **FNTz** (281 mg, 1.00 mmol) and trifluoroacetic acid (100 mL) in a 250-mL round-bottom flask, NBS (1.50 g, 8.42 mmol) was added at room temperature. After stirring for 16 h at 70 °C, the reaction mixture was quenched by the addition of water. After removal of the solvent by filtration, the residue was washed with methanol to give compound **FNTz-Br** (350 mg, 80%) as a yellow solid. MS (EI) *m/z* 437 (M$^+$); Anal. calcd for $C_{10}H_4Br_2F_2$: C 27.42, N 12.79; found: C 27.66, N, 12.83.

Synthesis of 6

FNTz-Br (100 mg, 0.23 mmol), 4-(2-ethylhexyl)-2-tributylstannylthiophene (1.00 g, 2.06 mmol), and Pd(PPh$_3$)$_4$ (30 mg, 0.031 mmol) were added to 30 mL of dry toluene in a flask. The reaction mixture was purged with N$_2$ for 15 min. Then, the mixture was refluxed for 12 h. After being cooled to room temperature, the reaction was quenched by the addition of H$_2$O. The aqueous layer was extracted with CHCl$_3$, and the combined organic layer was washed with water and dried over Na$_2$SO$_4$. After

removal of the solvent under reduced pressure, the residue was purified by column chromatography on silica gel (hexane/CHCl$_3$ = 1/1) to give **6** as a red solid (134 mg, 87%).^{1}H NMR (400 MHz, CDCl$_3$, δ): 8.21 (s, 2 H), 7.18 (s, 2 H), 2.64–2.62 (m, 4 H), 1.67–1.64 (m, 2 H) 1.40–1.28 (m, 16 H), 0.94–0.88 (m, 12 H); ^{13}C NMR (100 MHz, CDCl$_3$, δ): 156.8, 154.1, 152.8, 146.9, 142.5, 133.7, 131.3, 125.7, 115.8, 115.5, 113.9, 113.8, 40.5, 34.6, 32.6, 29.0, 25.7, 23.2, 14.3, 10.9; MS (MALDI-TOF) *m/z* 668.19 (M$^+$, Calcd 668.12); Anal. calcd for $C_{34}H_{38}F_2N_{24}S_4$: C 61.05, H 5.73, N 8.38; found: C 60.95, H 5.67, N, 8.34.

Synthesis of FNTz-T$_{eh}$-FA

Compound **6** (134 mg, 0.21 mmol) was added to 15 mL of THF in a flask. Then, NBS (89 mg, 0.50 mmol) was added in one portion. The reaction mixture was heated to 50 °C and stirred for 4 h. After being cooled to room temperature, the reaction was quenched by the addition of H$_2$O. The aqueous layer was extracted with CHCl$_3$, and the combined organic layer was washed with water and dried over Na$_2$SO$_4$. After removal of the solvent under reduced pressure, the residue was purified by column chromatography on silica gel with CHCl$_3$ as eluent to give intermediate **D** (dibromo compound) as a red solid (130 mg).^{1}H NMR (400 MHz, CDCl$_3$, δ): 7.99 (s, 2 H), 2.58–2.49 (m, 4 H), 1.68–1.62 (m, 2 H) 1.33–1.17 (m, 8 H), 1.11–0.98 (m, 8 H), 0.94–0.89 (m, 12 H). ^{13}C NMR (100 MHz, CDCl$_3$, δ): 156.7, 154.0, 152.2, 146.6, 142.0, 133.1, 131.4, 116.1, 115.3, 113.1, 113.0, 40.1, 34.0, 32.6, 28.9, 25.8, 23.2, 14.3, 10.9. This compound was used without further purification.

Pd(PPh$_3$)$_4$ (24 mg, 0.021 mmol) was added to a well-degassed solution of intermediate **D** (130 mg, 0.16 mmol) and **FA-B** (198 mg, 0.40 mmol) in toluene (10 mL) and 1 M K$_2$CO$_3$ aq. (1 mL). The resulting mixture was refluxed overnight. After being cooled to room temperature, the reaction was quenched by the addition of H$_2$O and extracted with CHCl$_3$. After removal of the solvent under reduced pressure, the residue was purified by preparative GPC to give **FNTz-T$_{eh}$-FA** as a red solid (182 mg, 65% (2 steps)). ^{1}H NMR (400 MHz, CDCl$_3$, δ): 8.45 (s, 2 H), 8.28 (s, 2 H), 8.24 (s, 2 H), 8.14–8.05 (m, 6 H), 7.83 (d, 2 H, J = 7.2 Hz), 7.72–7.68 (m, 2 H), 4.44–4.35 (m, 2 H), 2.65–2.56 (m, 4 H), 2.16–2.06 (m, 2 H), 1.80–1.75 (m, 2 H), 1.54 (d, 6 H, J = 6.8 Hz), 1.31–0.81 (m, 36 H), 0.66–0.60 (m, 12 H); ^{13}C NMR (100 MHz, CDCl$_3$, δ): 168.8, 144.6, 144.0, 141.3, 135.2, 135.1, 134.0, 133.2, 131.7, 131.4, 131.2, 129.6, 128.9, 127.9, 122.6, 121.9, 116.1, 47.7, 40.8, 33.9, 33.2, 32.5, 31.6, 28.6, 26.7, 25.8, 23.0, 22.6, 18.9, 14.1, 10.8; MS (MALDI-TOF) *m/z* 1402.5 (M$^+$, Calcd 1402.3); Anal. calcd. for

$C_{84}H_{80}F_2N_6O_4S_4$: C 71.87, H 5.74, N 5.99; found: C 71.68, H 5.94, N 5.85.

Photovoltaic device fabrication

Organic photovoltaic devices were prepared with a structure of indium tin oxide (ITO)/poly(3,4-ethylene-dioxythiophene:poly(styrenesulfonate) (PEDOT:PSS)/ active layer/Ca/Al. ITO-coated glass substrates were first cleaned by ultrasonication in toluene, acetone, water, and 2-propanol for 10 min each. ITO-coated glass substrates were then activated by ozone treatment for 1 h. PEDOT: PSS was spin-coated on the ITO surface at 3000 rpm for 1 min and dried at 135 °C for 10 min. The active layers were then prepared by spin-coating on the ITO/PEDOT: PSS electrode at 800 rpm for 1 min in a glove box. For P3HT:**FNTz-T$_{eh}$-FA** films, thermal annealing was performed at 140 °C for 10 min. The typical thickness of the active layer was 80–100 nm. Ca and Al electrodes were evaporated on the top of active layer through a shadow mask to define the active area of the devices (0.09 cm^2) under a vacuum of 10^{-5} Pa to a thickness of 30 and 100 nm, respectively, determined by a quartz crystal monitor. After sealing the device from the air, the photovoltaic characteristics were measured in air under simulated AM 1.5 G solar irradiation (100 mW cm^{-2}) (SAN-EI ELECTRIC, XES-301S). The current density (*J*)–voltage (*V*) characteristics of photovoltaic devices were measured by using a KEITHLEY 2400 source meter. The external quantum efficiency (EQE) spectra were measured by using a Soma Optics Ltd. S-9240. The thickness of active layer was determined by KLA Tencor Alpha-step IQ.

Space-charge-limited currents (SCLC) measurements

Double-carrier, hole-only and electron-only devices were prepared with a structure of Au (30 nm)/PEDOT:PSS (25 nm)/blend films/Ba (5 nm)/Al (100 nm), Au (30 nm)/ PEDOT:PSS (25 nm)/blend films/MoO$_3$ (10 nm)/Al (100 nm), and Al (30 nm)/blend films/Ba (5 nm)/Al (100 nm). Glass substrates were first cleaned by ultrasonication in water, acetone, and 2-propanol for 5 min each and then dried at 140 °C for 10 min. ITO-coated glass substrates were then activated by ozone treatment for 20 min. PEDOT:PSS was spin-coated on the glass surface at 2000 rpm for 10 s then at 4000 rpm for 60 s and then dried at 140 °C for 10 min. The active layers were prepared by the same procedure as that for the photovoltaic devices. MoO$_3$, Ba, and Al electrodes were evaporated on the top of active layer through a shadow mask to define the active area of the devices (0.01 cm^2) under a vacuum of 10^{-7} mbar to a thickness of 10, 5, or 100 nm, respectively, which was determined by a quartz crystal monitor.

Results and discussion

Design, synthesis, and thermal properties

We first calculated the molecular orbitals of **FNTz-T$_{eh}$-FA** together with those of **NTz-T$_{eh}$-FA** by density functional theory (DFT) at the B3LYP/6–31 G(d,p) level. To ease the calculation, all alkyl groups were replaced with methyl groups. As shown in Supplementary Fig. 1, both compounds have an almost planar structure with dihedral angles of less than 10°. In both cases, the HOMO and LUMO orbitals are localized in the central parts, while the HOMO-1, HOMO-2, LUMO + 1, and LUMO + 2 orbitals are localized in the terminal units. The fluorine atoms strongly participate in the LUMOs, and consequently, **FNTz-T$_{eh}$-FA** has a lower LUMO energy level and narrower HOMO–LUMO energy gap than **NTz-T$_{eh}$-FA**.

Two synthetic methods are known to construct the **NTz** framework: (1) the treatment of 1,5-dibromo-2,6-dihydroxynapthalene with tetrasulfur tetranitride (N$_4$S$_4$)[26] and (2) the formation of a thiadiazole ring using 1,2,5,6-tetraaminonapthalene and thionyl chloride (SOCl$_2$).[27] To follow method (1), we first synthesized a fluorine-introduced precursor (Supplementary Scheme 1). However, all attempts to synthesize **FNTz** resulted in the formation of complex mixtures, due to the high reactivity of fluorine atoms under the reaction conditions. Then, we turned our attention to method (2). However, conventional conditions to synthesize 1,2,5,6-tetraaminonapthalene were not applicable to the synthesis of 4,8-difluoro-1,2,5,6-tetraaminonapthalene, because the electron-withdrawing character of fluorine atoms changed the reactivity of substrates. After extensive screening of reagents and conditions, we succeeded in establishing the synthetic route for **FNTz**, which is based on the combination of imidation and nitration reactions to subsequently introduce four amino functional groups in the difluoronapthalene derivatives (Scheme 1). In this scheme, the protection of amino groups by a trifluoroacetyl group in compound **4** is also a key step to accomplish this route, since the introduction of other protecting groups led to difficulty in the following nitration and deprotection reactions. Treatment of **FNTz** with NBS in trifluoroacetic acid gave the dibromo compound **FNTz-Br**.

Since **FNTz-Br** showed limited solubility in organic solvents, we introduced a 2-ethylhexyl group to the thiophene linker to ensure solubility and obtained **6** by Stille coupling in a good yield. Finally, the Suzuki coupling reaction between **6** and **FA-B** was carried out using Pd (PPh$_3$)$_4$ as a catalyst to give the target compound **FNTz-T$_{eh}$-FA**. Reference compound **NTz-T$_{eh}$-FA** was obtained in a similar manner. The synthetic routes of counterparts **FA-B** and **NTz-T$_{eh}$-FA** are summarized in Supplementary Schemes 2 and 3. Both the target compounds are

Scheme 1 Synthesis of **FNTz** and **FNTz-T$_{eh}$-FA**
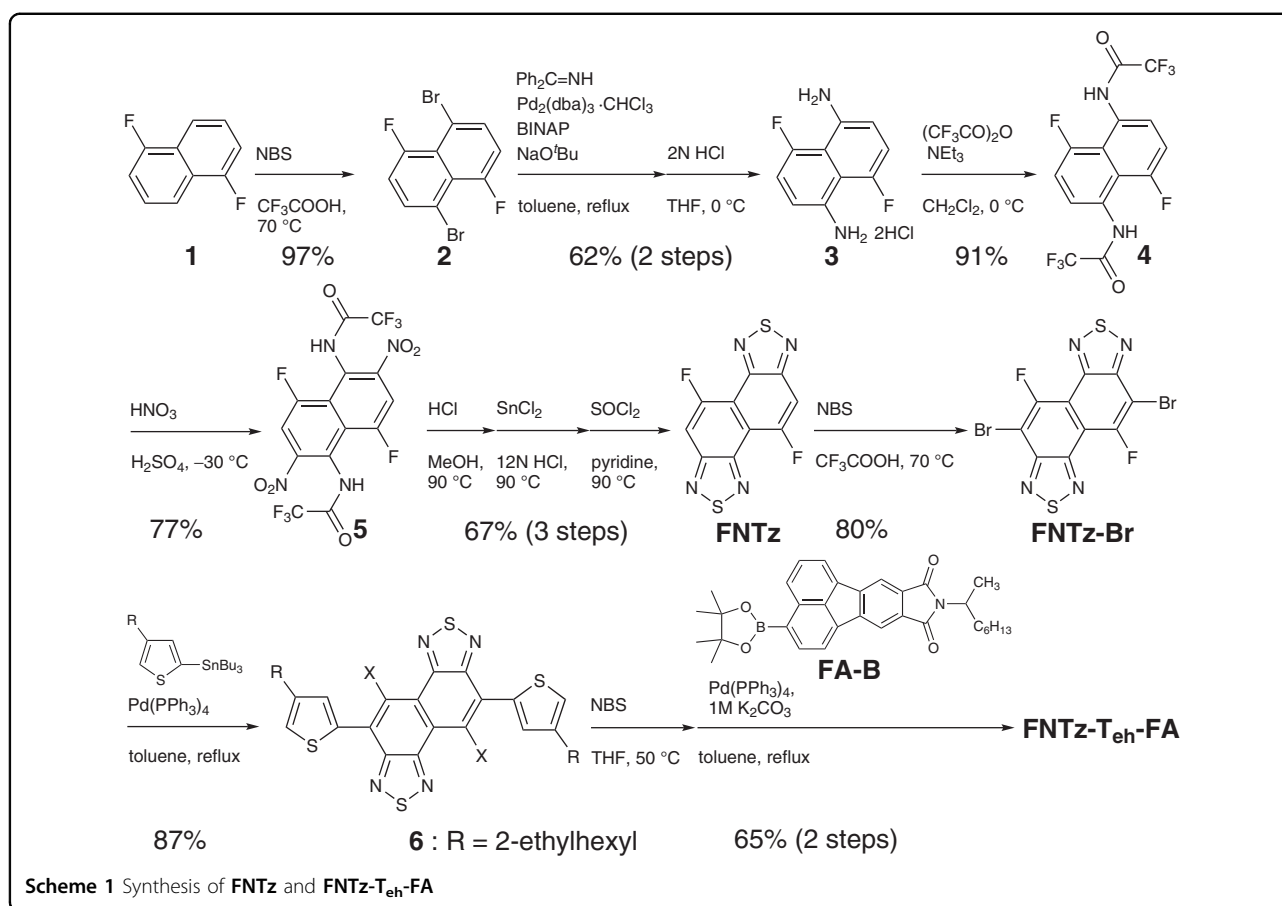
soluble in common organic solvents such as chloroform (CHCl$_3$), chlorobenzene (CB), and *o*-dichlorobenzene (*o*-DCB), which enables the physical properties to be examined in solution as well as in solution-processed device fabrication. Since we revealed that the presence of hexyl group is favorable for obtaining high short-circuit current against 2-ethylhexyl group,[19] we also synthesized **FNTz-T$_{hex}$-FA** and **NTz-T$_{hex}$-FA** with the hexyl group on the thiophene ring (chemical structure shown in Supplementary Fig. 2). However, the low solubility of **FNTz-T$_{hex}$-FA** precluded thin-film fabrication, indicating that the fluorine atoms in the **NTz** framework contribute to an increase in the intermolecular interactions. Characterization data of the new compounds using NMR, mass spectrometry, and elemental analysis are found in the Materials and Methods Section and Supplementary Information (SI).

Both acceptors are thermally stable with 5% weight loss temperatures (T_d) over 300 °C as confirmed by the TGA analysis (Supplementary Fig. 3a). This result indicates that the introduction of fluorine atoms into the **NTz** unit has little influence on the thermal stability. Melting peaks are obtained on the first heating of DSC curves of **FNTz-T$_{eh}$-FA** and **NTz-T$_{eh}$-FA** at 302 and 299 °C, respectively

(Supplementary Fig. 3b). For **NTz-T$_{eh}$-FA**, the melting peak remained steady in the second scan, indicating the partially crystallized behavior. XRD measurements of **NTz-T$_{eh}$-FA** film prepared by spin-coating from *o*-DCB solution showed weak signals, irrespective of the thermal annealing (Supplementary Fig. 4a). On the other hand, **FNTz-T$_{eh}$-FA** showed the transition from the amorphous to the crystalline phase at approximately 200 °C on the DSC curves. In fact, the spin-coated **FNTz-T$_{eh}$-FA** film showed a clear XRD peak after thermal annealing at 240 °C (Supplementary Fig. 4b). Note that **FNTz-T$_{eh}$-FA** retained an amorphous behavior at 140 °C, which corresponds to the typical OSC device fabrication conditions.

Physical properties

UV-vis absorption spectra of these compounds in a diluted CHCl$_3$ solution and thin films on quartz substrates are shown in Fig. 2, and the corresponding photophysical data are summarized in Table 1. The absorption maxima of **FNTz-T$_{eh}$-FA** and **NTz-T$_{eh}$-FA** in solution appeared at 525 and 509 nm, respectively. These bands mainly originate from the transition of the HOMO to LUMO, which is confirmed by the time-dependent

(TD) DFT calculations at the Coulomb-attenuating method (CAM)-B3LYP/6–31 G (d, p) level (see the SI). The absorption maximum of **FNTz-T$_{eh}$-FA** is redshifted compared to that of **NTz-T$_{eh}$-FA**. Based on the theoretical results (Supplementary Fig. 1), this phenomenon is explained by the relatively small HOMO–LUMO energy gap for **FNTz-T$_{eh}$-FA**. The molar extinction coefficient (ε) of **FNTz-T$_{eh}$-FA** is slightly larger than that of

NTz-T$_{eh}$-FA. The absorption spectra of the films are somewhat redshifted compared to those in the solution. The optical HOMO–LUMO energy gaps (ΔE_g^{opt}) of **FNTz-T$_{eh}$-FA** and **NTz-T$_{eh}$-FA** extracted from the absorption onset in the films are 2.08 and 2.13 eV, respectively. The absorption coefficients of the **FNTz-T$_{eh}$-FA** and **NTz-T$_{eh}$-FA** in the films were determined to be 7.2×10^3 and $5.5 \times 10^3 \, nm^{-1}$, respectively. This qualitative trend is in agreement with that of ε values.

The electrochemical behavior of **FNTz-T$_{eh}$-FA** and **NTz-T$_{eh}$-FA** was investigated by CV measurements in an o-DCB/acetonitrile (CH_3CN) (10:1) solution containing 0.1 M tetrabutylammonium hexafluorophosphate (TBAPF$_6$). The ferrocene/ferrocinium (Fc/Fc$^+$) redox couple was used as the internal standard for the calibration of redox potentials. Whereas no oxidation wave was detected within the potential window of the solvent, clear reversible multiple reduction waves were observed for both compounds (Fig. 3a), indicating that these molecules possess an electron-accepting nature. The observed good reversibility of each wave indicates that the formed anionic species of the **FNTz**-containing system are also kinetically stable under electrochemical conditions, which is an important requisite for stable charge transportation
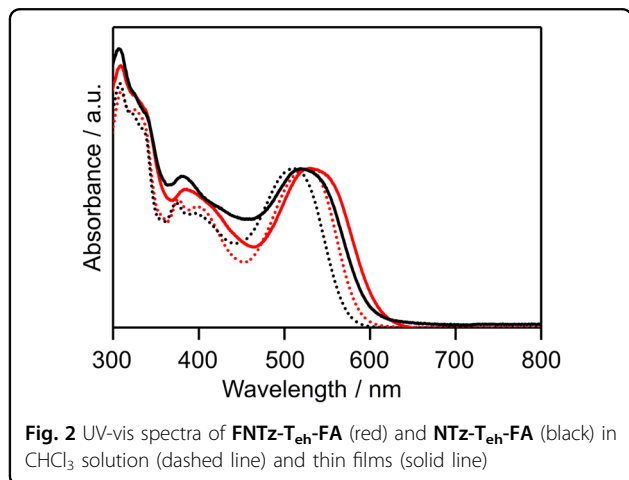

Fig. 2 UV-vis spectra of **FNTz-T$_{eh}$-FA** (red) and **NTz-T$_{eh}$-FA** (black) in CHCl$_3$ solution (dashed line) and thin films (solid line)

Table 1 Properties of nonfullerene acceptors

Acceptors	T_d / °C	λ_{max} / nm[a]	$^a\varepsilon$ / $M^{-1} \, cm^{-1}$	λ_{onset} / nm[b]	ΔE_g^{opt} / eV[c]	$E_{p.c.}$/ V[d]	E_{onset}^{red} / V[e]	E_{LUMO} / eV[f]	E_{HOMO} / eV[g]
FNTz-T$_{eh}$-FA	393	525	6.3×10^4	596	2.08	−1.17, −1.51, −1.70, −2.06	−1.25	−3.55	−6.17
NTz-T$_{eh}$-FA	412	509	6.1×10^4	580	2.13	−1.28, −1.50, −1.79, −2.06	−1.42	−3.38	−6.06

[a] In CHCl$_3$
[b] In film
[c] $\Delta E_{opt} = 1240 \, \lambda_{onset}^{-1}$
[d] Determined by DPV measurements
[e] Determined by CV measurements
[f] $E_{LUMO} = -E_{onset}^{red} - 4.80$
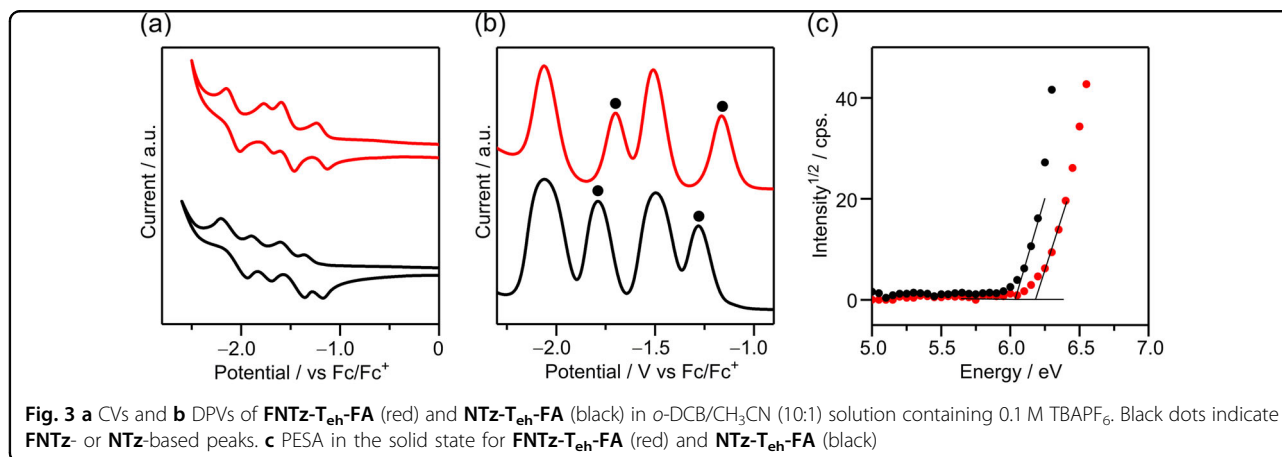[g] Determined by PESA measurements

Fig. 3 a CVs and **b** DPVs of **FNTz-T$_{eh}$-FA** (red) and **NTz-T$_{eh}$-FA** (black) in o-DCB/CH$_3$CN (10:1) solution containing 0.1 M TBAPF$_6$. Black dots indicate **FNTz**- or **NTz**-based peaks. **c** PESA in the solid state for **FNTz-T$_{eh}$-FA** (red) and **NTz-T$_{eh}$-FA** (black)

when utilized as an organic semiconducting material.[28] Each reduction potential ($E_{\text{p.c.}}$) of these compounds was determined by DPV (Fig. 3b) and is listed in Table 1. By comparison with the corresponding DPV waves of central and terminal units **6** and **8** (Supplementary Fig. 5), the first and third reduction peaks are assigned to the participation of **FNTz** unit. Importantly, the first reduction potential of **FNTz-T$_{\text{eh}}$-FA** is positively shifted compared to that of **NTz-T$_{\text{eh}}$-FA**, indicating that the **FNTz** unit has a stronger electron-accepting characteristic than **NTz**. Based on the onset of the first reduction wave in CV ($E_{\text{onset}}^{\text{red}}$) and the assumption that the energy level of Fc/Fc$^+$ is -4.8 eV below the vacuum level,[29] the LUMO energy levels (E_{LUMO}) of **FNTz-T$_{\text{eh}}$-FA** and **NTz-T$_{\text{eh}}$-FA** were estimated to be -3.55 and -3.38 eV, respectively. These values are qualitatively in good agreement with the theoretical results (Supplementary Fig. 1) and show sufficient driving force for charge separation when combined with P3HT (LUMO: -2.81 eV) as a donor. Based on the ionization potentials measured by the PESA in the film state, the HOMO energy levels (E_{HOMO}) of **FNTz-T$_{\text{eh}}$-FA** and **NTz-T$_{\text{eh}}$-FA** were determined to be -6.17 and -6.06 eV, respectively (Fig. 3c). These values also show a sufficient gap between the HOMO energy levels of the acceptor and P3HT (HOMO: -4.72 eV) for exciton dissociation via hole transfer to P3HT.

Photovoltaic characteristics

To evaluate the semiconductor performance of **FNTz-T$_{\text{eh}}$-FA** and **NTz-T$_{\text{eh}}$-FA**, bulk heterojunction solar cells with the conventional structure of ITO/PEDOT:PSS/active layer/Ca/Al were fabricated. The active layers were composed of a blend of P3HT as the donor and the newly synthesized π-conjugated compounds (**FNTz-T$_{\text{eh}}$-FA** and **NTz-T$_{\text{eh}}$-FA**) as acceptors. During the optimization of active layer fabrication, we noticed that *o*-DCB was the only possible solvent for the P3HT:**NTz-T$_{\text{eh}}$-FA** blend to fabricate thin films with the proper morphology. Thus, in order to provide a direct comparison between **FNTz-T$_{\text{eh}}$-FA** and **NTz-T$_{\text{eh}}$-FA**, we first optimized processing conditions using *o*-DCB as solvent with a blend composition at a 1:1 weight ratio and a concentration of 16 mg mL^{-1} for spin-coating, For the P3HT:**NTz-T$_{\text{eh}}$-FA** blend film, thermal annealing at 140 °C for 20 min was effective to improve photovoltaic characteristics. Under these conditions, the thicknesses of the active layers are distributed in a narrow range of 72–74 nm (Table 2), which facilitates comparison of the main factor for determining solar cell performance. The *J–V* characteristics of the devices under AM 1.5 G solar irradiation (100 mW cm^{-2}) and corresponding EQE spectra are shown in Fig. 4a, and the representative device parameters are summarized in Table 2 and Supplementary Tables 1–3. All supplementary

Table 2 Blend-film characteristics of the P3HT:acceptor films

Blend films	Solvent	Thickness / nm	J_{SC} / mA cm^{-2}	V_{OC} / V	FF / %	PCE / %[a]	μ_{eff} / m^2 V^{-1} s^{-1}	μ_{p} / m^2 V^{-1} s^{-1}	μ_{n} / m^2 V^{-1} s^{-1}
P3HT: NTz-T$_{\text{eh}}$-FA	*o*-DCB	72	2.13	0.95	53	1.06 (1.02 ± 0.02)	4.2 × 10^{-8}	2.2 × 10^{-8}	1.8 × 10^{-10}
P3HT: FNTz-T$_{\text{eh}}$-FA	*o*-DCB	74	4.44	0.89	52	2.05 (2.04 ± 0.02)	6.2 × 10^{-8}	6.5 × 10^{-9}	2.8 × 10^{-10}
P3HT: FNTz-T$_{\text{eh}}$-FA	CB	105	5.81	0.89	60	3.12 (3.02 ± 0.08)	8.8 × 10^{-8}	6.0 × 10^{-9}	2.5 × 10^{-10}

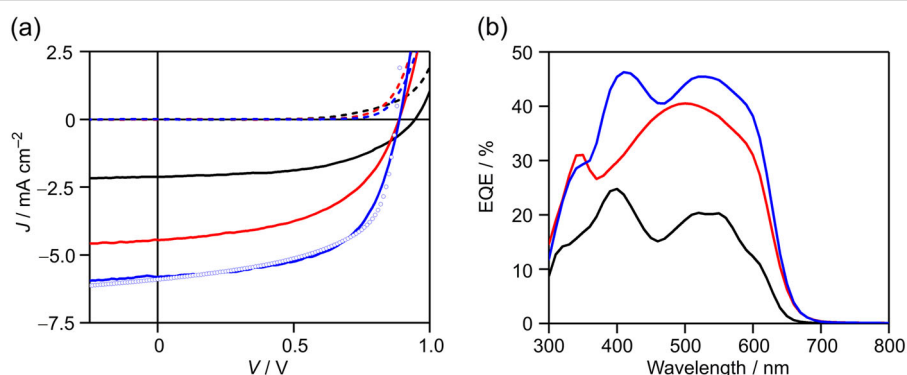[a]The average of six devices is provided in parentheses; see the SI for details

Fig. 4 a *J–V* characteristics under illumination (solid line) and in the dark (dashed line) and b EQE spectra for CB-processed P3HT:**FNTz-T$_{\text{eh}}$-FA** (blue), *o*-DCB-processed P3HT:**FNTz-T$_{\text{eh}}$-FA** (red) and *o*-DCB-processed P3HT:**NTz-T$_{\text{eh}}$-FA** (black). Simulated *J–V* curve of CB-processed P3HT:**FNTz-T$_{\text{eh}}$-FA** device is shown in the empty blue dot

J–*V* curves to confirm reproducibility are summarized in Supplementary Fig. 6.

Both blend films showed typical photovoltaic responses, indicating that these newly synthesized compounds functioned as acceptors. In correspondence with the relatively high-lying LUMO energy level for **NTz-T$_{eh}$-FA**, the open-circuit voltage (V_{oc}) of the P3HT:**NTz-T$_{eh}$-FA** device is higher than that of P3HT:**FNTz-T$_{eh}$-FA**. On the other hand, the short-circuit current density (J_{sc}) of P3HT:**FNTz-T$_{eh}$-FA** is roughly two times higher than that of P3HT:**NTz-T$_{eh}$-FA**. Overall, the P3HT:**FNTz-T$_{eh}$-FA**-based device showed a superior power conversion efficiency (PCE) of 2.05%. The EQE measurements showed that both devices exhibit a broad photoresponse between 300 and 700 nm (Fig. 4b). This result indicates that both donor and acceptor materials contribute to the photocurrent generation. To further optimize P3HT:**FNTz-T$_{eh}$-FA**-based devices, we screened the conditions and found that the use of CB solvent with a concentration of 36 mg mL^{-1} gave the highest PCE of 3.12%, with a J_{sc} of 5.81 mA cm^{-2}, V_{oc} of 0.89 V, and FF of 0.60. Under these conditions, the thickness of active layer was increased to 105 nm. The *J*–*V* curve and photovoltaic data of this device are shown in Fig. 4, Supplementary Fig. 6, and Table 2. In contrast to our previous **NTz**-based system, whose spin-coated solution required a mixed solvent system of CB/*o*-DCB with the volume ratio of 4:1,[17] the utilization of only CB showed an improved PCE for P3HT:**FNTz-T$_{eh}$-FA**. Furthermore, OSC devices based on P3HT and a representative fullerene acceptor, [6,6]-phenyl-C$_{61}$-butyric acid methyl ester (PC$_{61}$BM), showed a PCE of 2.68% under the same experimental setup and the same blend composition of the 1:1 ratio (Supplementary Fig. 7), indicating that **FNTz-T$_{eh}$-FA** has enough potential as an acceptor. The EQE spectrum of this device showed a photocurrent response with a maximum value of 47% at 420 nm. The J_{sc} value of 5.93 mA cm^{-2} estimated from the EQE spectrum was within 4.5% deviation from the observed value, indicating the accuracy of the photovoltaic measurement.
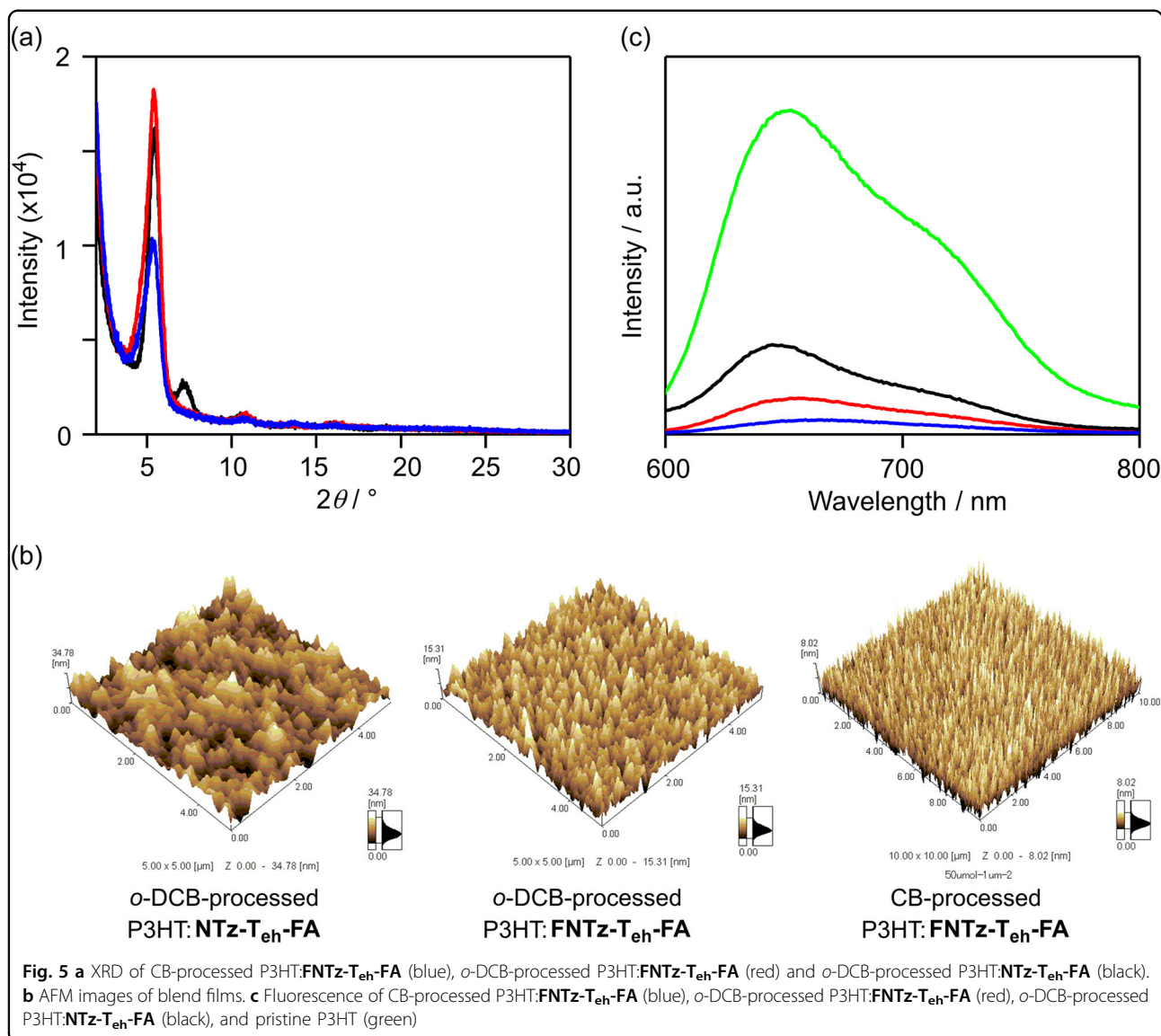
Blend-film evaluation

To identify the origin of improved performance for **FNTz-T$_{eh}$-FA**-based devices, properties of blend-films were investigated. The crystallinity of *o*-DCB-processed P3HT:**FNTz-T$_{eh}$-FA** and P3HT:**NTz-T$_{eh}$-FA** blend films, as well as a CB-processed P3HT:**FNTz-T$_{eh}$-FA** blend film, was investigated by XRD measurements. As shown in Fig. 5a, an XRD peak ascribable to the ordering of P3HT was observed at $2\theta = 5.0°$ for all the blend films.[30] An additional weak peak was found at $2\theta = 7.5°$ for the *o*-DCB-processed P3HT:**NTz-T$_{eh}$-FA** film. Since an XRD profile of pristine **NTz-T$_{eh}$-FA** film also displayed a weak diffraction peak at $2\theta = 7.5°$ (Supplementary Fig. 4a), we

determined that both P3HT and **NTz-T$_{eh}$-FA** have a crystalline nature in the blend films. On the other hand, under device fabrication conditions, **FNTz-T$_{eh}$-FA** retains amorphous behavior in both pristine and P3HT:**FNTz-T$_{eh}$-FA** blend films. We recently reported that the amorphous behavior of nonfullerene acceptors with linear structures is advantageous for effective charge separation due to the increased exposure of π-conjugated frameworks to the donor–acceptor (D–A) interfaces.[31]

To characterize the morphology of blend films, AFM was performed. As shown in Fig. 5b, the AFM height image of *o*-DCB-processed P3HT:**FNTz-T$_{eh}$-FA** film showed a relatively smooth surface with average roughness (R_a) of 2.33 nm, compared to that of P3HT:**NTz-T$_{eh}$-FA** films (4.96 nm). The use of CB solvent for P3HT:**FNTz-T$_{eh}$-FA** led to the smoother morphology with low R_a value of 1.58 nm. The relatively small R_a value of the P3HT:**FNTz-T$_{eh}$-FA** film indicates a favorable intermixing between the donor and acceptor with large domains, causing the good exciton dissociation.[17] The photoluminescence spectra of these blend films along with the pristine P3HT film, normalized by the fraction of their absorbed photons on excitation at the maximum absorption, are shown in Fig. 5c. The photoluminescence of all blend films was significantly quenched in comparison with a pristine P3HT film. The photoluminescence quenching efficiencies (PLQEs) of the blended films of *o*-DCB-processed P3HT:**FNTz-T$_{eh}$-FA** and P3HT:**NTz-T$_{eh}$-FA** relative to the PL intensities of P3HT film were calculated to be 89 and 73%, respectively. This result indicates that a more efficient photoinduced charge transfer from P3HT to **FNTz-T$_{eh}$-FA** occurred at the D–A interfaces.[31] The PLQE of the CB-processed P3HT:**FNTz-T$_{eh}$-FA** was increased to 95%, implying that the D–A interfaces of CB-processed films are further optimized relative to *o*-DCB-processed films. These results indicate that the P3HT:**FNTz-T$_{eh}$-FA** film possesses better morphologies for photovoltaic applications than the P3HT:**NTz-T$_{eh}$-FA** film.

A fundamental understanding of the device physics is important to develop **FNTz**-based nonfullerene acceptors. To investigate the effect of an electric field on the generated free carriers, we measured the photocurrent (J_{ph}) of CB-processed P3HT:**FNTz-T$_{eh}$-FA** blend film as a function of effective applied voltage (V_{eff}) under light intensities of 10 and 100 mW cm^{-2}. The photocurrent is defined by the equation $J_{ph} = J_L – J_D$, where J_L and J_D are the current density under illumination and dark conditions, respectively. The effective applied voltage is defined as $V_{eff} = V_0 – V$, where V_0 is the compensation voltage at $J_{ph} = 0$ and V is the applied bias. As shown in Fig. 6a, a square-root dependence of J_{ph} against V_{eff} is seen, which is characteristic of a recombination-limited photocurrent.[32] The J_{ph} does not fully saturate, even at high
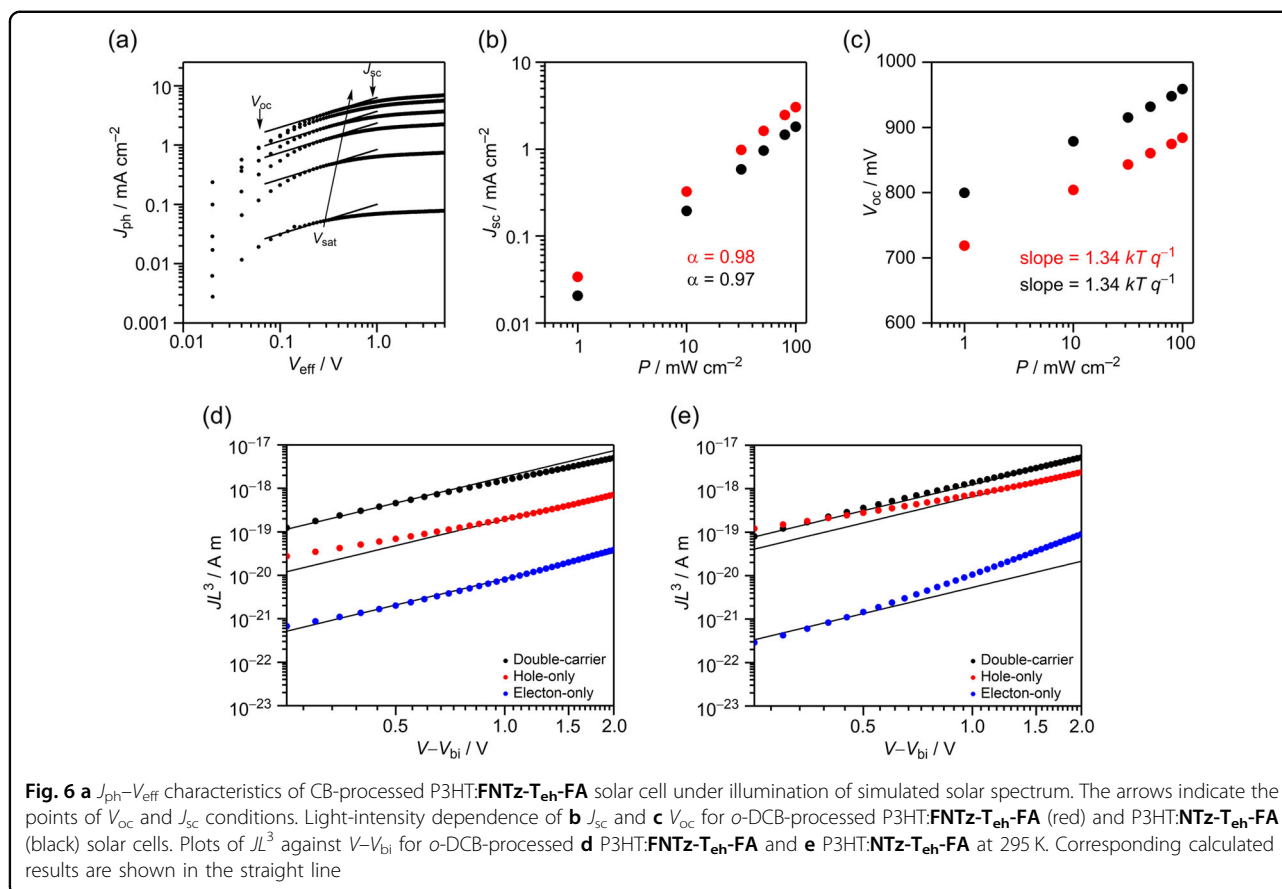
Fig. 5 a XRD of CB-processed P3HT:**FNTz-T$_{eh}$-FA** (blue), *o*-DCB-processed P3HT:**FNTz-T$_{eh}$-FA** (red) and *o*-DCB-processed P3HT:**NTz-T$_{eh}$-FA** (black). **b** AFM images of blend films. **c** Fluorescence of CB-processed P3HT:**FNTz-T$_{eh}$-FA** (blue), *o*-DCB-processed P3HT:**FNTz-T$_{eh}$-FA** (red), *o*-DCB-processed P3HT:**NTz-T$_{eh}$-FA** (black), and pristine P3HT (green)

effective voltages. This is explained by the presence of field-dependent geminate recombination. The maximum generation of free carriers (G_{max}) is estimated to be 3.98×10^{26} m^{-3} s^{-1} by using the saturated photocurrent (J_{ph}^{max}) and the equation:

$$J_{ph}^{max} = qG_{max}L$$

where q is the elementary charge and L, the layer thickness.

To investigate the influence of nongeminate recombination, the light-intensity (P) dependence of J_{sc} and V_{oc} under irradiation intensities between 1.0 and 100 mW cm^{-2} was found for *o*-DCB-processed P3HT:**FNTz-T$_{eh}$-FA** and P3HT:**NTz-T$_{eh}$-FA** devices. It has been established that the light-intensity dependence of J_{sc} can be

described with a power law according to $J_{sc} \propto P^{\alpha}$. A linear dependence of J_{sc} on P corresponds to $\alpha = 1$, where lower values of α indicate bimolecular recombination losses.[33–35] As shown in Fig. 6b, both devices showed $\alpha = 0.97$, where the small deviation from unity indicates that bimolecular recombination losses are not a major factor for both devices under short-circuit conditions. This result also indicates that the increasing J_{ph} beyond short-circuit conditions in Fig. 6a must be ascribed to a geminate-recombination process. To investigate the effect of trap-assisted recombination, we measured the light-intensity dependence of V_{oc}. It has been recognized that the slope of V_{oc} against the logarithm of P equals $kT\,q^{-1}$, where k is Boltzmann's constant, T is the temperature, and q is the elementary charge.[33,36] While the slope equals unity in the case of bimolecular recombination, this slope

Fig. 6 a J_{ph}–V_{eff} characteristics of CB-processed P3HT:**FNTz-T$_{eh}$-FA** solar cell under illumination of simulated solar spectrum. The arrows indicate the points of V_{oc} and J_{sc} conditions. Light-intensity dependence of **b** J_{sc} and **c** V_{oc} for o-DCB-processed P3HT:**FNTz-T$_{eh}$-FA** (red) and P3HT:**NTz-T$_{eh}$-FA** (black) solar cells. Plots of JL^3 against V–V_{bi} for o-DCB-processed **d** P3HT:**FNTz-T$_{eh}$-FA** and **e** P3HT:**NTz-T$_{eh}$-FA** at 295 K. Corresponding calculated results are shown in the straight line

increases in the presence of trap-assisted recombination.[37] As shown in Fig. 6c, both devices showed the same slope of $1.34 \, kT \, q^{-1}$. Interestingly, similar slopes were found for the P3HT:PC$_{61}$BM system, which was explained by a small contribution of trap-assisted recombination emphasized by the weak bimolecular recombination in this system.[38] The results of P dependence of J_{sc} and V_{oc} indicate that the presence of fluorine atoms in the π-conjugated systems used in this study has little influence on the recombination process.

To investigate the charge-transport characteristics and determine the bimolecular recombination rate, we measured SCLC in double-carrier, hole-only, and electron-only devices by using Au/PEDOT:PSS/active layer/Ba/Al, Au/PEDOT:PSS/active layer/MoO$_3$/Al, and Al/active layer/Ba/Al structures, respectively. A space-charge-limited current is described by

$$J = \frac{9}{8} \varepsilon \varepsilon_0 \mu \frac{V^2}{L^3}$$

where ε and ε_0 are relative and vacuum permittivity, and μ is the carrier mobility. The J–V characteristics of P3HT:**FNTz-T$_{eh}$-FA** and P3HT:**NTz-T$_{eh}$-FA** devices between 213 and 295 K are shown in Supplementary Fig. 8, and the plots of JL^3 for CB-processed films against V–V_{bi} at 295 K,

where L is the film thickness and V_{bi} is the built-in voltage, are shown in Fig. 6d, e. By using this equation, double-carrier (μ_{eff}), hole (μ_p), and electron (μ_n) mobilities of o-DCB-processed P3HT:**FNTz-T$_{eh}$-FA** film at 295 K were calculated to be 6.2×10^{-8}, 6.5×10^{-9}, and $2.8 \times 10^{-10} \, m^2 \, V^{-1} \, s^{-1}$, respectively (Table 2). Combining these mobilities by using the following equation:[39]

$$\gamma_{pre} = \frac{16\pi}{9} \frac{\mu_p \mu_n}{\mu_{eff}^2 - (\mu_p + \mu_n)^2}$$

estimates the Langevin prefactor (γ_{pre}), describing the deviation from the classical Langevin recombination rate. For o-DCB-processed P3HT:**FNTz-T$_{eh}$-FA** at 295 K, the Langevin prefactor is determined to be 2.7×10^{-3}, which is consistent with the low recombination losses in the solar cell, and remarkably similar to that of the P3HT:PC$_{61}$BM system. For P3HT:**NTz-T$_{eh}$-FA**, the hole mobility of $2.2 \times 10^{-8} \, m^2 \, V^{-1} \, s^{-1}$ is higher than P3HT:**FNTz-T$_{eh}$-FA**. On the other hand, the electron mobility is decreased to $1.8 \times 10^{-10} \, m^2 \, V^{-1} \, s^{-1}$. This unbalanced hole and electron mobility resulted in the lower double-carrier mobility ($4.2 \times 10^{-8} \, m^2 \, V^{-1} \, s^{-1}$) than P3HT:**FNTz-T$_{eh}$-FA**. These results indicate that the utilization of the **FNTz** unit contributes to improving the blend film

morphologies, leading to the efficient charge generation and transport for the P3HT:**FNTz-T$_{eh}$-FA** film. Finally, for CB-processed P3HT:**FNTz-T$_{eh}$-FA** film, the J–V characteristics of the solar cell can be simulated with a drift-diffusion model using G_{max},[40] the carrier mobilities estimated from Supplementary Figs. 8, 9, and γ_{pre} (1.1 × 10^{-3}). A density of states of $3.0 \times 10^{26}\,\text{m}^{-3}$ was used. As shown in Fig. 3a, simulated J–V characteristics in the presence of a field-dependent generation rate are in agreement with the experimental result, ascertaining the accuracy of values obtained in this study.

Summary

In summary, to develop a new strong electron-accepting unit based on the **NTz** framework, we designed a fluorine-substituted **NTz** and successfully synthesized it by the combination of sequential introduction of amino functional groups into 1,5-difluoronapthalene derivatives to form a fluorinated tetrafluoronapthalene derivative, followed by construction of thiadiazole rings using thionyl chloride. A new electron-accepting π-conjugated compound, **FNTz-T$_{eh}$-FA**, containing the **FNTz** as a central unit, was developed together with a reference compound of **NTz-T$_{eh}$-FA**, and applied as nonfullerene acceptors in OSCs. Photophysical and physicochemical measurements showed that the introduction of fluorine atoms in the **NTz** unit has considerable influence on the absorption behavior and frontier orbital energy levels of molecules. Organic solar cells based on the synthesized acceptors and P3HT as a donor showed that **FNTz-T$_{eh}$-FA** has superior performance to **NTz-T$_{eh}$-FA**, and a PCE up to 3.12% was attained. Blend-film investigations revealed that the P3HT:**FNTz-T$_{eh}$-FA** blend films showed good film morphologies, contributing to the efficient charge generation and transport characteristics. These results clearly demonstrate the high potential of **FNTz** as an electron-accepting unit, enabling us to develop new organic semiconductors containing **FNTz** units for application in donor–acceptor type donor and nonfullerene acceptor materials in OSCs. As a result, the utilization of **FNTz** can broaden the repertory of π-conjugated systems with high-performance and/or novel electronic functions, which can contribute to pave the way for the development and realization of organic electronics.

Author details
[1]The Institute of Scientific and Industrial Research, Osaka University, 8-1 Mihogaoka, Ibaraki, Osaka 567-0047, Japan. [2]Max Planck Institute for Polymer Research, Ackermannweg 10, 55128 Mainz, Germany. [3]Ishihara Sangyo Kaisha, Ltd., 3-1 Nishi-shibukawa 2-chome, Kusatsu, Shiga 525-0025, Japan

Competing interests
The authors declare no competing interests.

References
1. Shirota, Y. & Kageyama, H. Charge carrier transporting molecular materials and their applications in devices. *Chem. Rev.* **107**, 953–1010 (2007).
2. Li, Y. Molecular design of photovoltaic materials for polymer solar cells: toward suitable electronic energy levels and broad absorption. *Acc. Chem. Res.* **45**, 723–733 (2012).
3. Zhao, Y., Guo, Y. & Liu, Y. 25th anniversary article: recent advances in n-type and ambipolar organic field-effect transistors. *Adv. Mater.* **25**, 5372–5391 (2013).
4. Gao, X. & Hu, Y. Development of n-type organic semiconductors for thin film transistors: a viewpoint of molecular design. *J. Mater. Chem. C* **2**, 3099–3117 (2014).
5. Chen, W. & Zhang, Q. Recent progress in non-fullerene small molecule acceptors in organic solar cells (OSCs). *J. Mater. Chem. C* **5**, 1275–1302 (2017).
6. Li, H. et al. Fine-tuning the 3D structure of nonfullerene electron acceptors toward high-performance polymer solar cells. *Adv. Mater.* **27**, 3266–3272 (2015).
7. Kwon, O. K., Park, J.-H., Park, S. K. & Park, S. Y. Soluble dicyanodistyrylbenzene-based non-fullerene electron acceptors with optimized aggregation behavior for high-efficiency organic solar cells. *Adv. Energy Mater.* **5**, 1400929-1—6 (2015).
8. Liu, Y. et al. NDI-based small molecule as promising nonfullerene acceptor for solution-processed organic photovoltaics. *Adv. Energy Mater.* **5**, 1500195-1—5 (2015).
9. Holliday, S. et al. A rhodanine flanked nonfullerene acceptor for solution-processed organic photovoltaics. *J. Am. Chem. Soc.* **137**, 898–904 (2015).
10. Lee, J. et al. A nonfullerene small molecule acceptor with 3D interlocking geometry enabling efficient organic solar cells. *Adv. Mater.* **28**, 69–76 (2016).
11. Zhao, W. et al. Molecular optimization enables over 13% efficiency in organic solar cells. *J. Am. Chem. Soc.* **139**, 7148–7151 (2017).
12. Wang, M. et al. Donor–acceptor conjugated polymer based on naphtho[1,2-c:5,6-c]bis[1,2,5]thiadiazole for high-performance polymer solar cells. *J. Am. Chem. Soc.* **133**, 9638–9641 (2011).
13. Osaka, I. et al. Synthesis, characterization, and transistor and solar cell applications of a naphthobisthiadiazole-based semiconducting polymer. *J. Am. Chem. Soc.* **134**, 3498–3507 (2012).
14. Liu, Y. et al. Aggregation and morphology control enables multiple cases of high-efficiency polymer solar cells. *Nat. Commun.* **5**, 5293 (2014).
15. Vohra, V. et al. Efficient inverted polymer solar cells employing favourable molecular orientation. *Nat. Photonics* **9**, 403–409 (2015).
16. Osaka, I. & Takimiya, K. Naphthobischalcogenadiazole conjugated polymers: emerging materials for organic electronics. *Adv. Mater.* **29**, 1605218-1—20 (2017).

17. Chatterjee, S., Ie, Y., Karakawa, M. & Aso, Y. Naphtho[1,2-*c*:5,6-*c′*]bis[1,2,5]thia-diazole-containing π-conjugated compound: nonfullerene electron acceptor for organic photovoltaics. *Adv. Funct. Mater.* **26**, 1161–1168 (2016).

18. Chatterjee, S., Ie, Y. & Aso, Y. Influence of terminal imide units on properties and photovoltaic characteristics for benzothiadiazole-based nonfullerene acceptors. *J. Photopolym. Sci. Technol.* **30**, 557–560 (2017).

19. Chatterjee, S., Ie, Y. & Aso, Y. Naphtho[1,2 −*c*:5,6 −*c′*]bis[1,2,5]thiadiazole-based nonfullerene acceptors: effect of substituents on the thiophene unit on properties and photovoltaic characteristics. *ACS Omega* **3**, 5814–5824 (2018).

20. Ie, Y., Sasada, S., Karakawa, M. & Aso, Y. Pyradinodithiazole: an electron-accepting monomer unit for hole-transporting and electron-transporting conjugated copolymers. *Org. Lett.* **17**, 4580–4583 (2015).

21. Zhou, H. et al. Development of fluorinated benzothiadiazole as a structural unit for a polymer solar cell of 7% efficiency. *Angew. Chem. Int. Ed.* **50**, 2995–2998 (2011).

22. Zhang, Y. et al. Increased open circuit voltage in fluorinated benzothiadiazole-based alternating conjugated polymers. *Chem. Commun.* **47**, 11026–11028 (2011).

23. Min, J., Zhang, Z.-G., Zhang, S. & Li, Y. Conjugated side-chain-isolated D–A copolymers based on benzo[1,2-b:4,5-b′]dithiophene-alt-dithienylbenzo-triazole: synthesis and photovoltaic properties. *Chem. Mater.* **24**, 3247–3254 (2012).

24. Albrecht, S. et al. Fluorinated Copolymer PCPDTBT with enhanced open-circuit voltage and reduced recombination for highly efficient polymer solar cells. *J. Am. Chem. Soc.* **134**, 14932–14944 (2012).

25. Reichenbächer, K., Süss, H. I. & Hulliger, J. Fluorine in crystal engineering—"the little atom that could". *Chem. Soc. Rev.* **34**, 22–30 (2005).

26. Mataka, S. et al. Sulfer nitride in organic chemistry. Part 19. Selective formation of benzo- and benzobis[1,2,5]thiadiazole skeleton in the reaction of tetrasulfur tetranitride with naphthalenols and related compounds. *Bull. Chem. Soc. Jpn.* **64**, 68–73 (1991).

27. Kawashima, K., Osaka, I. & Takimiya, K. Effect of chalcogen atom on the properties of naphthobischalcogenadiazole-based π-conjugated polymers. *Chem. Mater.* **27**, 6558–6570 (2015).

28. Liu, T. & Troisi, A. What makes fullerene acceptors special as electron acceptors in organic solar cells and how to replace them. *Adv. Mater.* **25**, 1038–1041 (2013).

29. Cardona, C. M., Li, W., Kaifer, A. E., Stockdale, D. & Bazan, G. C. Electrochemical considerations for determining absolute frontier orbital energy levels of conjugated polymers for solar cell applications. *Adv. Mater.* **23**, 2367–2371 (2011).

30. Erb, T. et al. Correlation between structural and optical properties of com-posite polymer/fullerene films for organic solar cells. *Adv. Funct. Mater.* **15**, 1193–1196 (2005).

31. Jinnai, S. et al. Electron-accepting π-conjugated systems for organic photo-voltaics: influence of structural modification on molecular orientation at donor–acceptor interfaces. *Chem. Mater.* **28**, 1705–1713 (2016).

32. Lenes, M., Morana, M., Brabec, C. J. & Blom, P. W. M. Recombination-limited photocurrents in low bandgap polymer/fullerene solar cells. *Adv. Funct. Mater.* **19**, 1106–1111 (2009).

33. Cowan, S. R., Roy, A. & Heeger, A. J. Recombination in polymer-fullerene bulk heterojunction solar cells. *Phys. Rev. B* **82**, 245207-1−10 (2010).

34. Schilinsky, P., Waldauf, C. & Brabec, C. J. Recombination and loss analysis in polythiophene based bulk heterojunction photodetectors. *Appl. Phys. Lett.* **81**, 3885–3887 (2002).

35. Mihailetchi, V. D., Xie, H., de Boer, B., Jan Anton Koster, L. & Blom, P. W. M. Charge transport and photocurrent generation in poly(3-hexylthiophene): methanofullerene bulk-heterojunction solar cells. *Adv. Funct. Mater.* **16**, 699–708 (2006).

36. Koster, L. J. A., Mihailetchi, V. D., Ramaker, R. & Blom, P. W. M. Light intensity dependence of open-circuit voltage of polymer:fullerene solar cells. *Appl. Phys. Lett.* **86**, 123509-1−3 (2005).

37. Mandoc, M. M., Veurman, W., Jan Anton Koster, L., de Boer, B. & Blom, P. W. M. Origin of the reduced fill factor and photocurrent in MDMO-PPV:PCNEPV all-polymer solar cells. *Adv. Funct. Mater.* **17**, 2167–2173 (2007).

38. Wetzelaer, G.-J. A. H., Kuik, M. & Blom, P. W. M. Identifying the nature of charge recombination in organic solar cells from charge-transfer state electro-luminescence. *Adv. Energy Mater.* **2**, 1232–1237 (2012).

39. Wetzelaer, G.-J. A. H., Van der Kaap, N. J., Jan Anton Koster, L. & Blom, P. W. M. Quantifying bimolecular recombination in organic solar cells in steady state. *Adv. Energy Mater.* **3**, 1130–1134 (2013).

40. Koster, L. J. A., Smits, E. C. P., Mihailetchi, V. D. & Blom, P. W. M. Device model for the operation of polymer/fullerene bulk heterojunction solar cells. *Phys. Rev. B* **72**, 085205-1–9 (2005).